

## Stress-guided lightweight design and optimisation for 3D printing sacrificial moulds

Wenpeng Xu<sup>a</sup>, Ning Zhang<sup>a</sup>, Hao Xu<sup>a,b,\*</sup>, Liuchao Jin<sup>c,\*</sup>, Jingchao Jiang<sup>d,\*</sup>

<sup>a</sup> School of Computer Science Technology, Henan Polytechnic University, Jiaozuo, 454003, China

<sup>b</sup> School of Computer Science and Technology, Shandong University, Qingdao, 266237, China

<sup>c</sup> Department of Mechanical and Automation Engineering, The Chinese University of Hong Kong, Hong Kong, China

<sup>d</sup> Department of Engineering, University of Exeter, Exeter, EX4 4QF, UK

### ARTICLE INFO

**Keywords:**

3D printing  
Sacrificial moulds  
Lightweight structures  
Injection moulding  
Sustainability

### ABSTRACT

3D printing has become widely-applied for manufacturing sacrificial moulds. However, conventional mould designs often involve simple geometries like cube, leading to excessive material usage and high production costs. The moulds will need to be removed after casting, resulting in wasted mould material. Currently, with the development of additive manufacturing technologies, complex and light-weight mould structures can be fabricated easily with a low cost. Therefore, this study proposes a stress-guided lightweight design methodology for 3D printing sacrificial moulds. The approach begins by applying an outward offset to the target model, generating a uniform-thickness shell with the inner surface aligning with the target model's geometry. The shell thickness is then optimised based on stress distribution to ensure that the mould can withstand fluid pressure during injection moulding, forming a non-uniform thickness shell model. The potential leakage problem due to 3D printing interlayer gaps is also considered and optimised in our proposed method. Experimental validation demonstrates that the optimised shell model achieves accurate casting of the target geometry. Compared to traditional cube-shaped sacrificial moulds, it achieves up to 94.7% reduction in volume, 95.01% material saving, and 83% improvement in fabrication time, all while maintaining structural stability. This method offers a practical solution for cost-effective and efficient 3D printing sacrificial mould design.

### 1. Introduction

Lightweighting has become an important strategy across various industries for enhancing material efficiency and minimising safety-related risks [1,2]. This study builds on this principle, focusing on the lightweighting in the sacrificial mould industry. Sacrificial moulds are temporary tools used in manufacturing processes, which are removed or dissolved after forming or manufacturing is complete to obtain the final product [3]. Historically, sacrificial moulds have been widely employed since ancient times for producing complex metal castings in jewelry and sculpture [4,5]. In modern manufacturing, sacrificial moulds play a pivotal role across diverse sectors including medical [6–10], electronics [11,12], automotive [13], and aerospace sectors [14]. Unlike reusable moulds, sacrificial moulds offer unique advantages for fabricating complex models. They eliminate the need for splitting the model to enable demoulding and do not require consideration of mould durability. Moreover, the flexibility to use various materials—including plastics

[15–18], metals [19–27], and composites [28–34]—enhances their versatility [35]. Sacrificial moulds also support rapid forming with isotropic properties that ensure quality and performance in the final product [36]. Therefore, they are widely adopted in applications requiring complex shapes or high customisation, especially for one-time or small-batch production.

Despite their advantages, traditional methods of manufacturing sacrificial moulds, such as machining and handcrafting, face some challenges. These methods are often costly and time-intensive compared to reusable moulds, and they are unsuitable for highly complex geometries or innovative designs [1]. These limitations have driven the need to explore advanced technologies to improve efficiency and reduce the cost of sacrificial mould production.

3D printing provides a transformative solution to these challenges faced by sacrificial mould production. This additive manufacturing (AM) technology constructs objects layer by layer, using materials like plastics that can bond together [37–44]. This technique not only effectively

\* Corresponding authors.

E-mail addresses: [haoxu5640@gmail.com](mailto:haoxu5640@gmail.com) (H. Xu), [liuchao.jin@link.cuhk.edu.hk](mailto:liuchao.jin@link.cuhk.edu.hk) (L. Jin), [J.Jiang2@exeter.ac.uk](mailto:J.Jiang2@exeter.ac.uk) (J. Jiang).

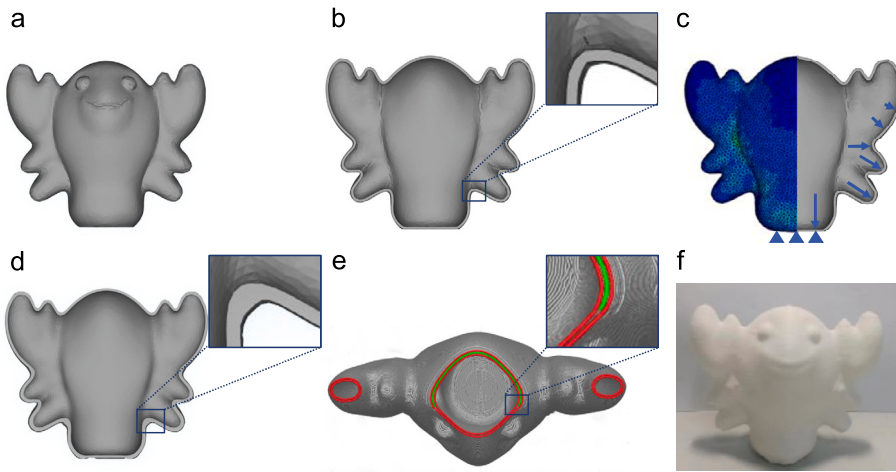


**Fig. 1. Overview of the proposed algorithm.** (a) Input 3D model. (b) Uniform-thickness shell model generated based on the minimum printable thickness, with a magnified view highlighting the consistent shell thickness. (c) Finite element analysis results, showing the applied boundary conditions for liquid pressure, where arrow length indicates the magnitude of the load. (d) Non-uniform thickness shell model after stress-guided optimisation, with a magnified view illustrating variations in shell thickness. (e) Contour optimisation for improved manufacturability, with a magnified view showing the increased number of printing paths. (f) Final printed mold model (external supports removed for visualisation).

reduces mould weight but also provides advantages like easy customisation, suitability for complex shapes, and rapid prototyping, which strongly promotes the development of personalised product design and manufacturing [45], mechanical structure design [37,46–48], and 3D reconstruction [49]. In mould manufacturing [50–58], especially in sacrificial mould production, 3D printing shows significant potential. Relevant research on 3D printing materials and processes has also laid the groundwork for the fabrication of sacrificial moulds [59–62]. In recent years, the application of 3D printing in sacrificial mould design has made substantial progress. For example, Montero et al. [63] introduced a method for creating dissolvable AM customised sacrificial moulds using polyvinyl alcohol (PVA) filament. After resin injection and curing, the mould is dissolved in the water, leaving behind a solid resin part. Wick-Joliat et al. [64] used 3D printing to create water-soluble sacrificial moulds for ceramic injection moulding, achieving the first successful production of sacrificial moulds on a fused deposition modelling (FDM) printer using PVA for high-quality model manufacturing. Jiang et al. [65] reported a novel strategy for fabricating the complex and multifunctional components of low-melting-point alloy (LMPA) by extrusion AM with two nozzles. One nozzle is used for printing the mould, and the other is for injecting LMPA. Although these studies successfully manufactured complex products, most sacrificial moulds remain cubic in shape, with limited consideration for lightweight designs that could reduce material usage and print time. This not only results in material waste and low printing efficiency but also exacerbates resource consumption and waste generation, placing greater pressure on the environment. Thus, this study introduces, for the first time, a lightweight design approach for 3D printed sacrificial moulds, aiming to reduce material usage while ensuring mould strength.

Therefore, this study proposes a stress-guided lightweight design method for 3D printing sacrificial moulds. This method first generates a uniform-thickness shell by processing the target model to produce an inner surface that matches the outer surface of the target model. Next, to ensure that the mould can withstand the liquid pressure during injection moulding, the shell thickness is adjusted based on stress distribution, resulting in a stress-guided shell model. Moreover, the method addresses the issue of liquid leakage that can arise from interlayer gaps inherent to 3D printing structures during the pouring process. Following these optimisations, the shell model is fabricated using 3D printing, and the manufacturing process is validated through experimental testing of the proposed approach. This is a straightforward and practical method for 3D printing sacrificial moulds design.

The main contributions are summarised as follows:

- A stress-guided lightweight design method for 3D printing sacrificial moulds is proposed, which incorporates variable wall thickness based on stress distribution to effectively mitigate stress concentrations caused by structural issues of the model or liquid pressure. This approach minimises material waste in the mould manufacturing process while ensuring structural integrity.
- A mould fabrication method using a dual-extruder FDM 3D printer was developed, in which dual-material printing was employed to produce both the mould shell and the removable support structures. The sacrificial moulds fabricated through this process enabled successful casting of models with LMPA, thereby demonstrating the effectiveness and adaptability of the proposed method.

## 2. Methodology

### 2.1. Algorithm overview

A stress-guided lightweight optimisation method for sacrificial mould design is presented, with the overall process illustrated in Fig. 1. First, starting from a given 3D solid model  $M$  in Fig. 1(a), a shell model  $M'_0$  with a uniform thickness is built to satisfy the minimum printable thickness  $t_{min}$  of the 3D printer, and the inner surface matches the surface of  $M$  (in Fig. 1(b)). To account for the liquid pressure exerted on the mould during the casting process, finite element analysis (FEA) is conducted on the shell model  $M'_0$ , with boundary conditions and simulation results illustrated in Fig. 1(c). Stress data  $\sigma = \{\sigma_1, \sigma_2, \dots, \sigma_n\}$  are extracted from the nodes  $e = \{e_1, e_2, \dots, e_n\}$  on the outer surface of  $M'_0$ . Each node's stress  $\sigma_i$  is evaluated against the yield strength constraint ( $\sigma_i \leq \sigma_y$ ). If there are nodes that fail to satisfy this constraint, the positions of certain outer surface nodes will be translated along the surface normal direction to increase the shell thickness at those locations to create an updated model  $M'_1$ . This process is iteratively repeated until all nodes satisfy the yield strength constraint. After  $k$  iterations, the shell model  $M'_k$  is obtained. The final non-uniform thickness shell model  $M'$ , meeting the stress constraints, is shown in Fig. 1(d).

For the shell model, interlayer gaps created during 3D printing slicing will compromise the integrity of the mould, leading to potential leakage or structural failure during casting. To solve this problem, this study continues to optimise the thickness of the shell model from the view of the 3D-printed sliced layer by means of point offsets, the result after slicing is shown in Fig. 1(e), resulting in a manufacturable mould with minimal volume and satisfying all constraints. The final printed mould is shown in Fig. 1(f). Note that the external supports are easily

removed. Therefore, the shell model in the figure is displayed without external support.

## 2.2. Stress-guided lightweight mould optimisation

### 2.2.1. Stress analysis

The lightweight mould design method in this study employs stress analysis to guide the iterative adjustment of mould thickness, utilising stress distribution data to evaluate the optimisation results and determine the feasibility of further improvements. We use plastic materials, the von Mises yield criterion is used to determine whether the material enters a state of plastic deformation. According to this criterion, yielding occurs when the von Mises equivalent stress at a point within the material exceeds a critical threshold, indicating the onset of plastic deformation. This stress  $\sigma$ , derived from the shear strain energy, is calculated using the principal stresses  $[\sigma_{p_1}, \sigma_{p_2}, \sigma_{p_3}]$  of the node  $e$  as follows:

$$\sigma = \sqrt{\frac{1}{2} \left[ \left( \sigma_{p_1} - \sigma_{p_2} \right)^2 + \left( \sigma_{p_2} - \sigma_{p_3} \right)^2 + \left( \sigma_{p_3} - \sigma_{p_1} \right)^2 \right]}. \quad (1)$$

To evaluate the stress distribution within the model, the von Mises stress is computed for all regions of the model and compared against the material's yield strength  $\sigma_y$ . To ensure structural safety, the material's yield strength is divided by a safety factor  $N$  greater than 1, establishing an allowable stress level that serves as a design constraint to guarantee structural integrity. For plastic materials, the allowable stress is defined as:

$$\sigma_{\max} \leq \frac{\sigma_y}{N}. \quad (2)$$

Similarly, in this study, a safety factor  $S$  not greater than 1 is adopted as the coefficient of the yield strength. Accordingly, the yield strength constraint incorporating the safety factor is formulated as:

$$\sigma_{\max} \leq S \cdot \sigma_y, \quad (3)$$

where  $\sigma_{\max}$  is the maximum stress in all nodes. The safety factor  $S$  accounts for uncertainties and ensures that  $S \leq 1$ . If the working stress exceeds this limit, the component is deemed unsafe.

In this study, a FEA is performed on the mould during the static phase after liquid injection in the casting process. The specific steps include tetrahedral meshing of the model, configuring the physical environment, applying a load perpendicular to the inner surface of the model, and fixing the bottom for static analysis, as shown in Fig. 1(c). Finally, the derived stress distribution results are used as input for subsequent modelling processes.

### 2.2.2. Stress-guided generation of non-uniform thickness shells

Thin shell structures are widely recognised for their material efficiency. However, thin shells often lack the structural strength necessary to withstand operational loads. To address this limitation and ensure sufficient strength under liquid pressure during injection moulding, a shell design with non-uniform thickness is proposed. This method optimises material usage while maintaining the structural integrity of the mould.

First, the given model undergoes surface offset processing to generate a uniformly thick shell model. This model consists of inner and outer surfaces, with the inner surface matching the original model, while the outer surface is generated through a rapid surface offset algorithm [66], where the offset distance corresponds to the shell thickness. However, the uniformly thick shell model cannot guarantee that the von Mises stress at all nodes remains within the material's allowable stress range, which may lead to mould damage during the injection moulding process.

Therefore, this study introduces a stress-based thickness optimisation method. Since the inner surface must remain consistent with the original model, the thickness optimisation is achieved by adjusting the

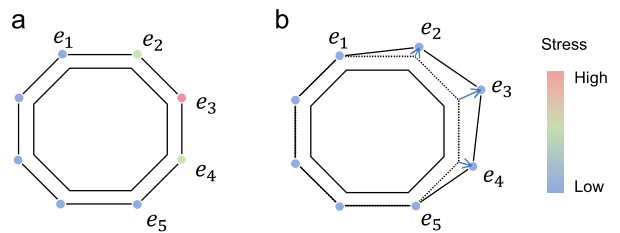


**Fig. 2. Vertex stress-based offset map.** (a) Initial shape. (b) Shape after outward displacement along the normal direction.

shape of the outer surface. Specifically, based on the stress distribution calculated through FEA, the outer surface nodes are shifted along their normal directions: nodes with higher stress have larger offsets, while nodes with lower stress have smaller offsets. Fig. 2 demonstrates this outward offset process. For example, in Fig. 2(a), nodes  $e_1$  and  $e_5$  do not satisfy the offset criteria and remain stationary, whereas nodes  $e_2$ ,  $e_3$ , and  $e_4$  are adjusted. Node  $e_3$ , experiencing the highest stress, undergoes the largest displacement, whereas nodes  $e_2$  and  $e_4$  experience smaller displacements. The resultant shell configuration following these adjustments is depicted in Fig. 2(b). This iterative process continues until the stress at all nodes fall below the yield strength of the material. The specific details of this method are described below.

The outward offset of nodes requires accurate computation of the normal vector  $\vec{N}_{e_i}$  at each vertex. The normal is calculated as the weighted average of the normal vectors of all faces connected to the vertex, with the weights determined by the area of the respective faces. This approach ensures that larger faces contribute more significantly to the vertex normal. If a vertex is connected to  $n$  faces, each with a normal vector  $\vec{N}_j$  and an area  $A_j$ , the vertex normal is computed as follows:

$$\vec{N}_{e_i} = \frac{\sum_{j=1}^n A_j \vec{N}_j}{\sum_{j=1}^n A_j}. \quad (4)$$

The movement distance  $d_i$  for each outer surface vertex along its normal direction during each iteration is calculated using the following formula:

$$d_i = \left( \frac{\sigma_i}{\sigma_a} - 1 \right) \cdot \alpha, \quad (5)$$

where  $\sigma_a$  denotes the average stress of all nodes in the model for the current iteration. Deviations from the global average stress are utilised to guide localised shell thickness adjustments, thereby promoting structural balance, avoiding excessive material buildup, and enhancing overall performance. The inclusion of  $\sigma_a$  ensures smoother results by normalising the stress distribution across the model. The parameter  $\alpha$  determines the step precision for updating node coordinates. Smaller values of  $\alpha$  improve accuracy at the cost of increased iterations, whereas larger values reduce iteration counts but may compromise the precision of the final model.

The updated position  $e'_i$  of an external point  $e_i$ , after being displaced by distance  $d_i$ , is given by:

$$e'_i = e_i + \frac{\vec{N}_{e_i}}{\|\vec{N}_{e_i}\|} \cdot d_i. \quad (6)$$

Based on the above, this study proposes an algorithm for generating a shell with non-uniform thickness based on stress distribution, as shown in Algorithm 1.

Despite the small and adjustable displacement distances in each iteration, the normal-direction offsetting of outer surface nodes may result in self-intersections within the model. To mitigate this issue, a self-intersection removal algorithm [67], originally developed for triangular mesh offsetting, is employed after each iteration. This self-intersection removal algorithm operates by starting from valid triangles and em-

**Algorithm 1:** Generation of Non-Uniform Thickness Shell Based on Stress.

```

Input: Given model  $M$ .
Output: Non-uniform thickness shell  $M'$ .
Apply the rapid surface offset algorithm to the given model  $M$  to
generate an initial uniform thickness shell  $M'_0$ ;
 $\text{FEA}(M'_0)$ ;
while maximum stress  $\sigma_{\max} > S \cdot \sigma_y$  do
    Calculate the normals of the outer surface nodes of model  $M'_k$ ;
    //  $M'_k$  is the non-uniform thickness shell of the
    //  $k$ -th iteration
    for each outer node  $e_i$  of  $M'_k$  do
        if the stress value at the node  $\sigma_i > \sigma_a$  then
            Calculate the normal vector  $\vec{N}_{e_i}$  and the movement distance
             $d_i$  using Equation (4) and (5);
            Update the moved point to  $e'_i$  using Equation (6);
        end
    end
     $\text{FEA}(M'_k)$ ;
    Update  $\sigma_{\max}$ ;
     $k++$ ;
end

```

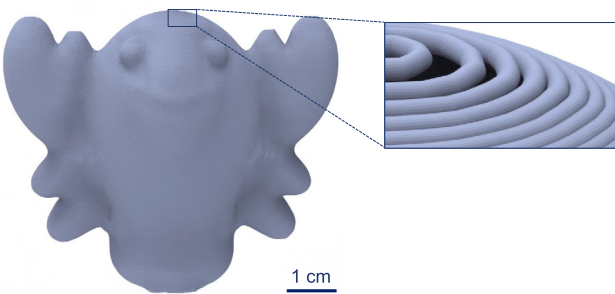


**Fig. 3.** Demonstration of interlayer gaps within a thin-shell structure.

ploying a region-growing technique. It traverses only valid and partially valid regions, bypassing invalid or self-intersecting areas. By iteratively addressing self-intersecting regions, the algorithm generates a consistent, non-self-intersecting mesh, ensuring the structural integrity and geometric fidelity of the final shell model.

### 2.3. Interlayer gap treatment

The fundamental principle of 3D printing involves fabricating three-dimensional objects by sequentially stacking material layers, with each layer requiring a stable foundation on the preceding one. However, during the slicing process, interlayer gaps may emerge when the surface inclination angle (defined as the angle between the tangent to the surface and the  $X-Y$  plane) is too small. These gaps are particularly problematic in planar slicing Fig. 3 illustrates this issue using a simulated thin-shell printing path, accompanied by an enlarged view of a section where gaps are clearly visible. It can be observed that, due to the steep curvature at the top of the model during layer-by-layer printing, the deposition paths between adjacent layers cannot fully overlap, resulting in the formation of interlayer gaps.

In general 3D printed models, especially those with internal filling structure, such interlayer gaps are often inconsequential and overlooked because they have minimal impact on printing quality. Nonetheless, some studies have sought to address this issue through non-planar printing or adaptive layer thickness techniques [68–70]. However, this gap is very detrimental to thin shell moulds. These defects can compromise not only the structural integrity and print quality but also the functionality of the mould, potentially causing leakage during the casting process and severely degrading the quality of the final product.

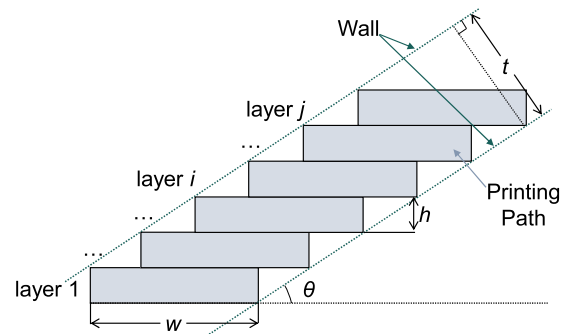


**Fig. 4.** Schematic diagram of the cross-section of the printing path.

To address this issue, manufacturability constraints must be integrated into the design phase. This ensures that the model's manufacturability and structural integrity are maintained, preventing the formation of gaps. Therefore, this section proposes an improved design optimisation strategy. By selectively adjusting the thickness of the model in regions prone to gaps, the proposed method effectively prevents gap formation, avoids leakage, and enhances the performance and reliability of thin-shell moulds during both printing and casting.

The cross-section of the printing path is simplified into a rectangular representation, as shown in Fig. 4. Here,  $i$  and  $j$  denote layers  $i$  and  $j$ , respectively, from the bottom to the top,  $\theta$  represents the inclination angle,  $h$  is the layer height,  $t$  represents the wall thickness of the shell, and  $w$  is the width of the printer nozzle's extrusion path (the width of the fill path).

The occurrence of gaps can be described as follows: when the wall thickness  $t$  remains constant, gaps form if the inclination angle  $\theta$  is less than a critical value. For example, in Fig. 5(a), when  $\theta$  is sufficiently large, the wall thickness  $t$  ensures tight connections between printing paths. In contrast, as  $\theta$  decreases to a threshold value (Fig. 5(b)), the wall thickness  $t$  is in a critical state, just unable to meet the connection requirements between printing paths. Gaps easily appear between printing layers and do not meet mould manufacturing requirements. As  $\theta$  further decreases to the scenario in Fig. 5(c), the wall thickness  $t$  no longer meets the printing requirement, leading to gaps between paths.

To address the above issue, a thickness adjustment strategy has been developed. This strategy dynamically modifies the wall thickness in regions with low inclination angles, establishing a direct correlation between the inclination angle  $\theta$  and the required thickness  $t$ , where  $t$  is given by the following equations:

$$t = n \cdot w \sin \theta + \delta, \quad (7)$$

where  $n$  is the number of printing paths needed and  $w$  is the width of the printing paths. The path width  $w$  is a fixed value, and the value of  $n$  can be derived from the critical condition, as illustrated in Fig. 5(d). Under this condition,  $t = nw \sin \theta$  (in the figure,  $n = 2$ ) and  $t = h \cos \theta$ . However, as  $n$  must be an integer in practical applications, the derived value of  $n$  shall be rounded up to the nearest integer to ensure complete and adequate coverage. By equating these expressions, Equation (8) is obtained.

$$n = \lceil \frac{h}{w \tan \theta} \rceil. \quad (8)$$

At the same time, the printing path cross-section is not rectangular but elliptical or another shape [71]. Therefore, we introduce a small deviation term  $\delta$  to represent this discrepancy, which is neglected in the calculation due to its minimal impact. From Equations (7) and (8), it can be concluded that smaller angles  $\theta$  require more number of paths  $n$ , i.e., thicker shell model thickness  $t$ . Fig. 5 shows a comparison schematic before and after treatment by the above method. Fig. 5(d) demonstrates the local thickness of the optimised shell model and the number of paths after slicing. It can be clearly seen that the number of paths after slicing

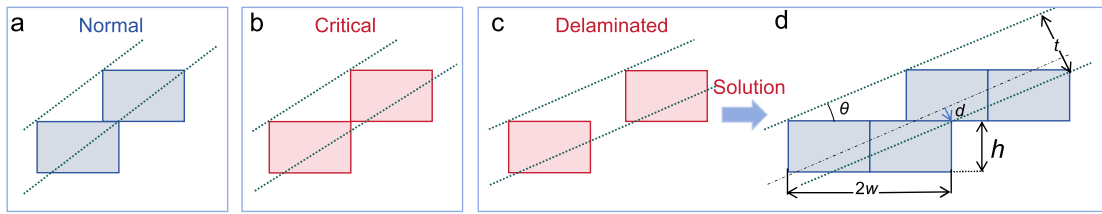


**Fig. 5. The effect of printing angle and the wall thickness on thin shell printing.** (a) When the printing angle is  $\theta$ , the wall thickness  $t$  meets the printing requirements. (b) The angle  $\theta$  decreases to the point where the wall thickness  $t$  is in a critical state, which just does not meet the connection requirements between the print paths. (c) Further reduction of  $\theta$  results in the appearance of gaps. Blue indicates regions that are successfully printable, while red denotes areas where printing fails. (d) Schematic diagram of the interlayer gap treatment for Fig. 5(c).

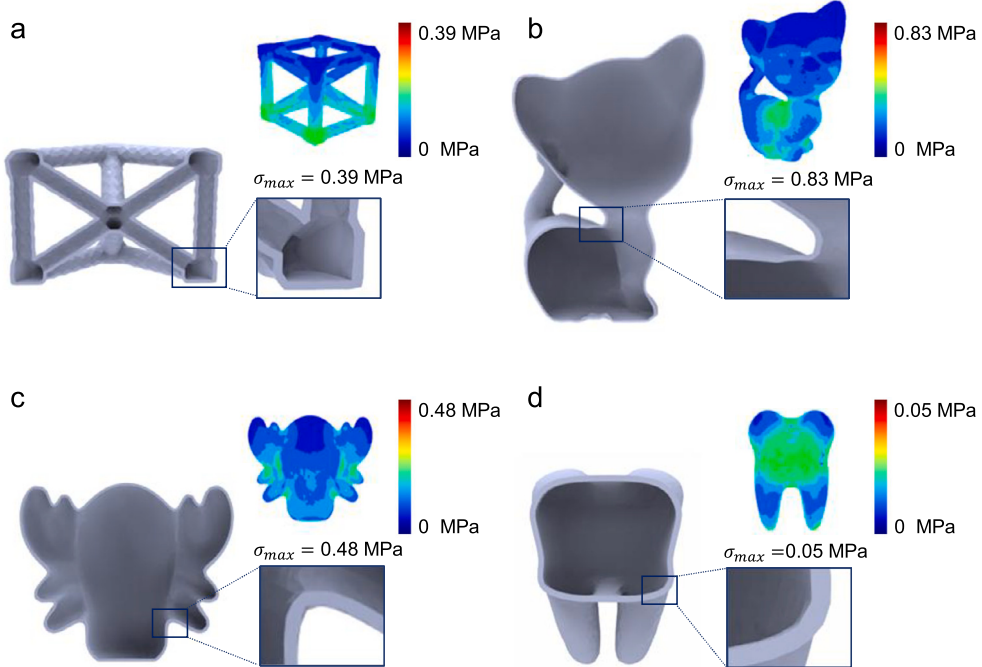


**Fig. 6. Moulds and FEA results under unpressurized conditions.** (a) Lattice model. (b) Kitten model. (c) Wawa model. (d) Tooth model.

increases due to the increased thickness of the shell model, which leads to the disappearance of interlayer gaps.

The method of thickening the shell model is similar to Section 2.2. The difference is that the reference is not the stresses at the nodes after FEA, but the angle  $\theta$  between the vectors of the inner surface nodes and the horizontal plane. Once the angle of each inner surface node's vector is determined, the nearest outer surface node along the opposite direction of its normal is found, and then the thickness of the shell model in the current localised region is increased by offsetting the position of the outer surface node. Where the distance  $d$  by which the outer surface node is offset is the localised thickness calculated through Equation (7) minus the current localised thickness of the shell model.

### 3. Results and discussion

This section details the calculation results of the lightweight mould of solid models of varying geometric complexity, the results of manufacturing, and comparison with the traditional method. The method was evaluated using Polylactic acid (PLA) as the printing shell material, PVA as the printing support material, and LMPA as the casting material, respectively. The proposed method is highly generalisable and adaptable. The materials and 3D printing process employed in this study were selected for experimental validation purposes; however, they can be flexibly substituted with alternative printing materials and manufac-

turing techniques as needed, to accommodate different casting scenarios and application requirements.

#### 3.1. Calculation results

The algorithm was implemented using Python on a PC equipped with an Intel Core i7-11700 CPU operating at 2.5 GHz and 16 GB of memory. PLA was selected as the shell printing material, with a density of 1.24 g/cm<sup>3</sup>, an elastic modulus of 2750 MPa, a Poisson's ratio of 0.36, and a yield strength of 70 MPa. The relevant coefficients for the analysis were set as the safety factor  $S = 0.7$  and the step precision  $\alpha = 0.2$ . To ensure printing feasibility and structural integrity, the initial uniform shell thickness was set to 0.8 mm, although the theoretical minimum thickness achievable in FDM 3D printing could be thinner.

Our method was validated on a large number of 3D models—four of them were selected to demonstrate the effectiveness of the proposed method, as demonstrated in Fig. 6 and 9. The dimensions and key information for these models are summarised in Table 1. To evaluate the generalizability of the proposed method, experiments were conducted under two distinct scenarios: unpressurized and pressurized conditions.

##### 3.1.1. Unpressurized experimental conditions

In the first scenario, the unpressurized condition represents gravity casting. Here, the pressure at the base of the model depends on the model height and the density of the LMPA, calculated using the hydrostatic pressure formula:

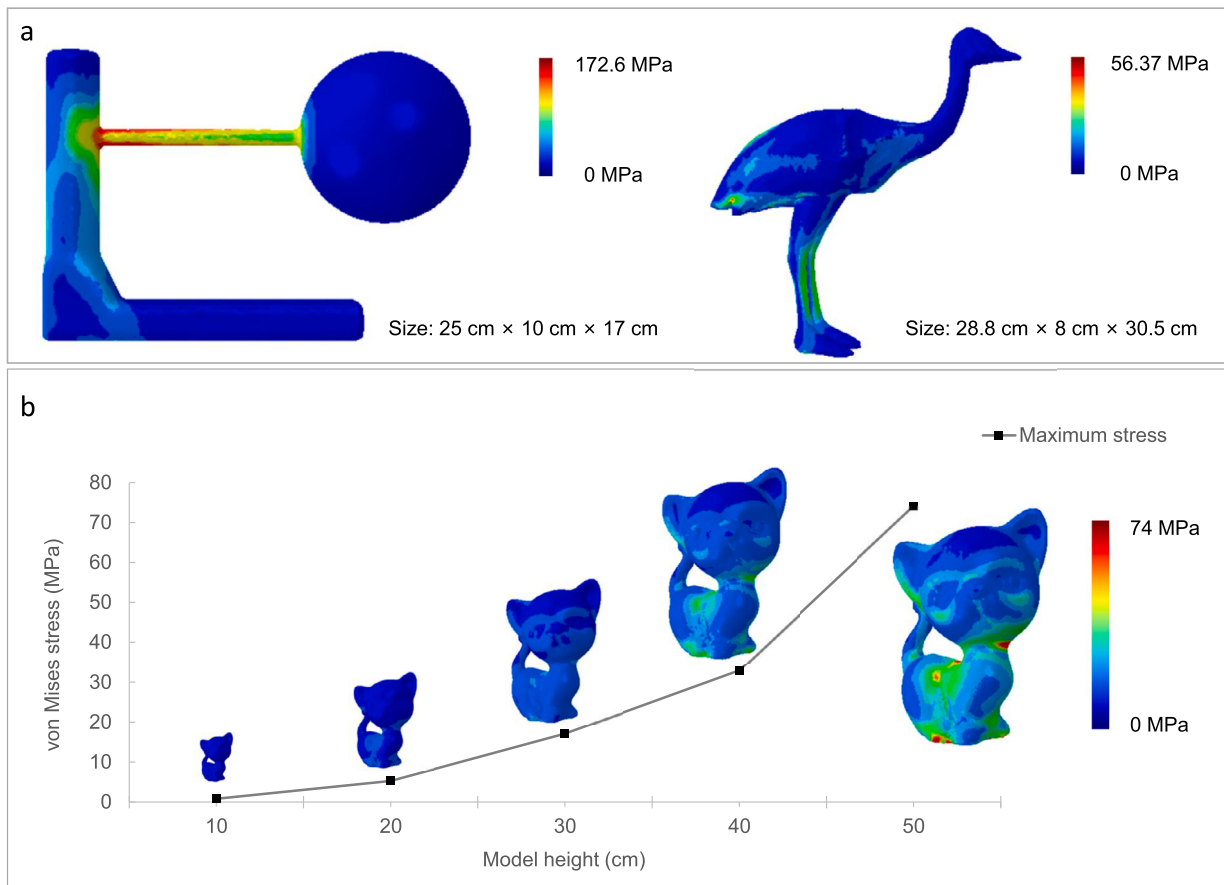


**Fig. 7. FEA results for specialised models and scaled models under unpressurized conditions. (a)** Stress analysis of the Hanging-Ball model and Flamingo model. **(b)** Stress variations in Kitten models of increasing size.

**Table 1**

The information statistics of the models tested under pressurized experimental conditions.

Model	Size [mm]	No. of Nodes	No. of Iterations
Kitten	67.2 x 61.2 x 101.6	20568	7
Lattice	70.0 x 70.0 x 50.0	5639	4
Wawa	66.3 x 33.1 x 55.0	9399	5
Tooth	21.5 x 22.3 x 29.2	2772	0

$$p = \rho g h, \quad (9)$$

where  $p$  represents pressure,  $\rho$  is the material density,  $g$  is the acceleration due to gravity, and  $h$  is the vertical distance from the node to the liquid surface's highest point. The density of the LMPA is 9.2 g/cm<sup>3</sup>.

The calculation results of the unpressurized experimental conditions are shown in Fig. 6, which includes four shell cross-sections, the finite element analysis results, and the maximum stress values. As illustrated in the figure, all maximum stress values remain below the material's yield strength. The analysis showed that the initial shell thickness of 0.8 mm was sufficient to withstand the liquid pressure during manual pouring. The maximum stress is well below the material's yield strength (i.e.,  $S \cdot \sigma_y = 49$  MPa). Therefore, no additional iterations were required for shell thickness adjustment in this condition, resulting in zero iterations.

For static injection moulding or small-scale moulds, generating a uniformly thick shell at the initial stage is often sufficient to meet the design requirements. This outcome represents a specific application of the proposed algorithm and serves as a simplified case within its broader framework. However, for more complex or larger models, stress distribution must still be carefully evaluated. For example, in the Hanging Ball model shown in Fig. 7(a) (with dimensions annotated in the figure), the suspended nature of the geometry leads to significant stress concentration in the support area. As a result, even under static casting conditions, the initial shell thickness is insufficient to satisfy structural requirements, and iterative optimisation is still necessary. Similarly, the Flamingo model in Fig. 7(a) also fails to meet casting requirements under static pressure. Its slender supporting legs are primary regions of stress concentration. Although the overall size of the model is comparable to other cases, local stress near the connection areas exceeds the yield strength of PLA, thus requiring further thickness optimisation. Moreover, the geometric scale of the model directly affects the magnitude of maximum stress. As illustrated in Fig. 7(b), the maximum stress in identical models (e.g., the Kitten model) increases progressively with model size. These findings underscore the critical role of stress analysis in the lightweight design of sacrificial moulds with complex geometries. By continuing with the subsequent algorithmic steps, effective lightweight mould designs can still be achieved through the generation of non-uniform shell thickness.

To further validate the effectiveness of the proposed method, a sacrificial mould for the Hanging Ball model was designed under static pressure using the approach described in this study, as shown in the Fig. 8.

### 3.1.2. Pressurized experimental conditions

The second scenario involves high-pressure casting, a widely utilised process for LMPA, particularly in the automotive industry, accounting for approximately 60% of all castings [72]. This method minimises impurity deposition and flow marks, prevents air bubble formation, and enhances the consistency and surface quality of castings.

To meet the demands of high-pressure casting, pressure simulations were conducted using conditions representing 150 times standard hy-

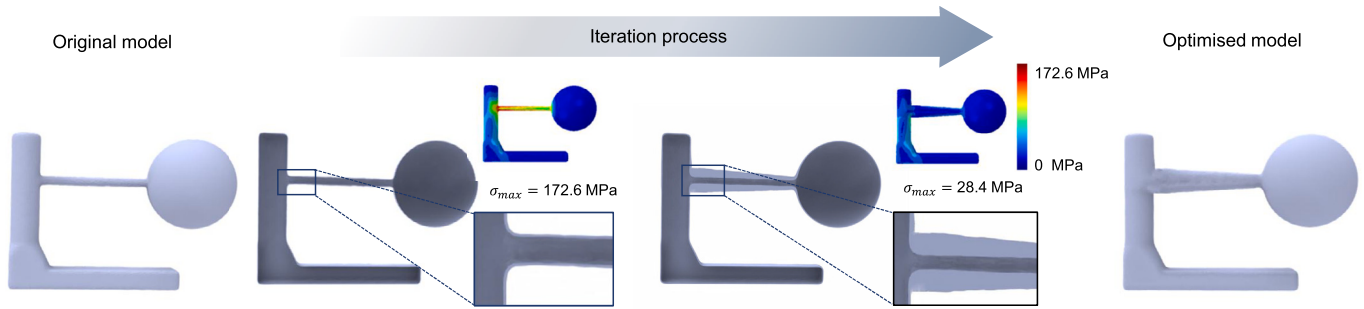


Fig. 8. Design results of the sacrificial mould for the Hanging Ball model under static pressure.

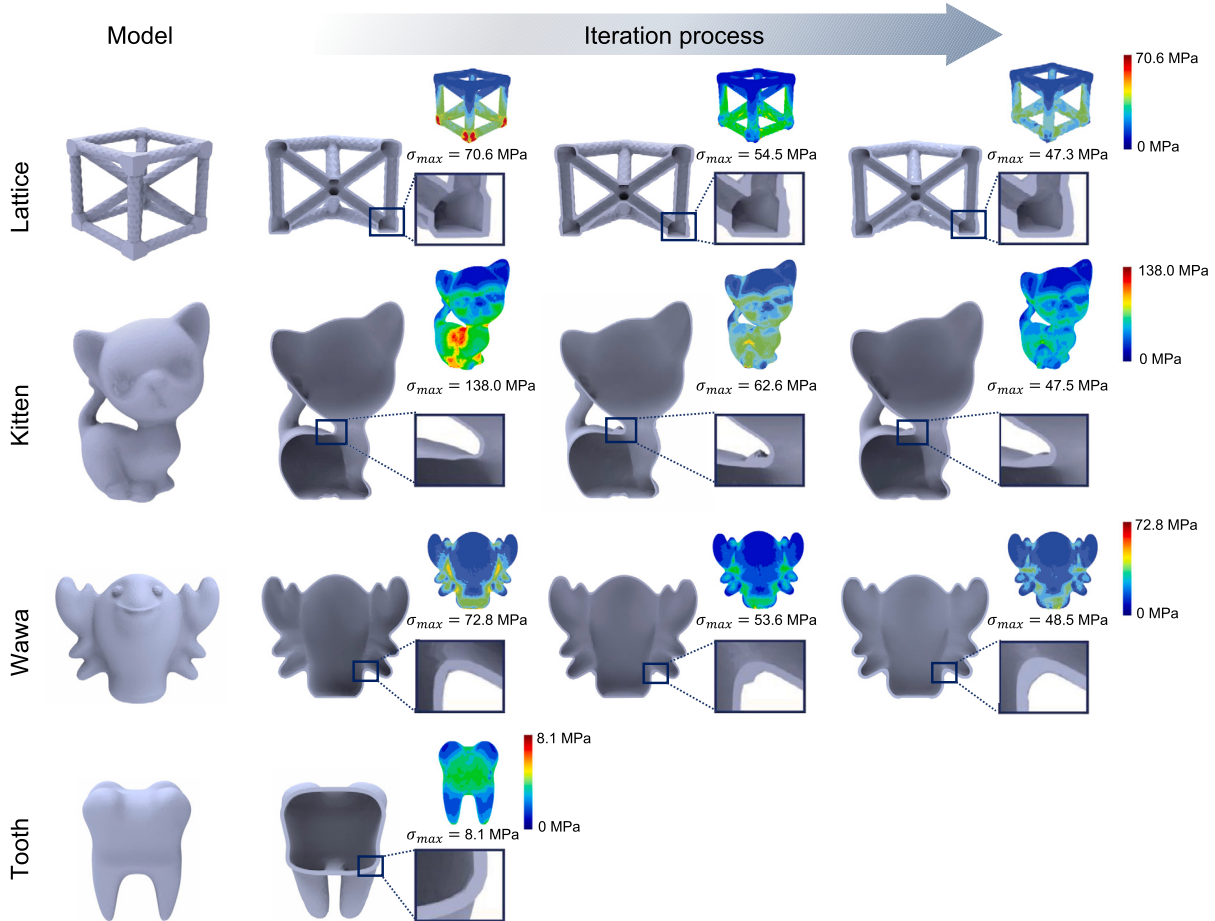


Fig. 9. Models and FEA results under pressurized conditions. From left to right, the images represent the input model ( $M$ ), the uniform-thickness shell ( $M'_0$ ), intermediate iterations ( $M'_k$ ), and the final optimised shell model ( $M'$ ).

draulic pressure. The computational results under pressurized experimental conditions are illustrated in Fig. 9. From left to right, this figure displays the input model ( $M$ ), the uniform-thickness shell ( $M'_0$ ), intermediate iterative adjustments ( $M'_k$ ), and the final optimised result ( $M'$ ). The stress evolution throughout the optimisation process is depicted in Fig. 10, which shows the variations in both maximum and average stress across iterations.

A combined analysis of Figs. 9 and 10 demonstrates that the average stress consistently decreased with each iteration, and the maximum stress was successfully reduced below the yield strength threshold after a maximum of seven iterations. Notably, the tooth model, due to its exceptionally small dimensions, achieved structural stability with the minimum printable thickness, even under pressurized conditions.

The runtime of the proposed algorithm is primarily constrained by the stress analysis performed during each iteration, which typically re-

quires 5 to 10 minutes per cycle. The algorithm's performance is influenced not by the physical size of the model but by the number of nodes in the mesh; models with a higher node count generally demand longer computation times. Across all experiments presented in this paper that involved iterative optimisation, the maximum recorded runtime was 70 minutes, with an average of approximately 30 minutes.

### 3.2. Physical evaluation

The physical evaluation begins with a solid 3D mesh model designated for casting and develops a sacrificial mould specifically for injection moulding. The design process involves reinforcing the shell thickness based on stress distribution analysis, followed by optimisation to ensure the manufacturability of the 3D printing process. The final output is a shell model tailored for casting applications. For the location of

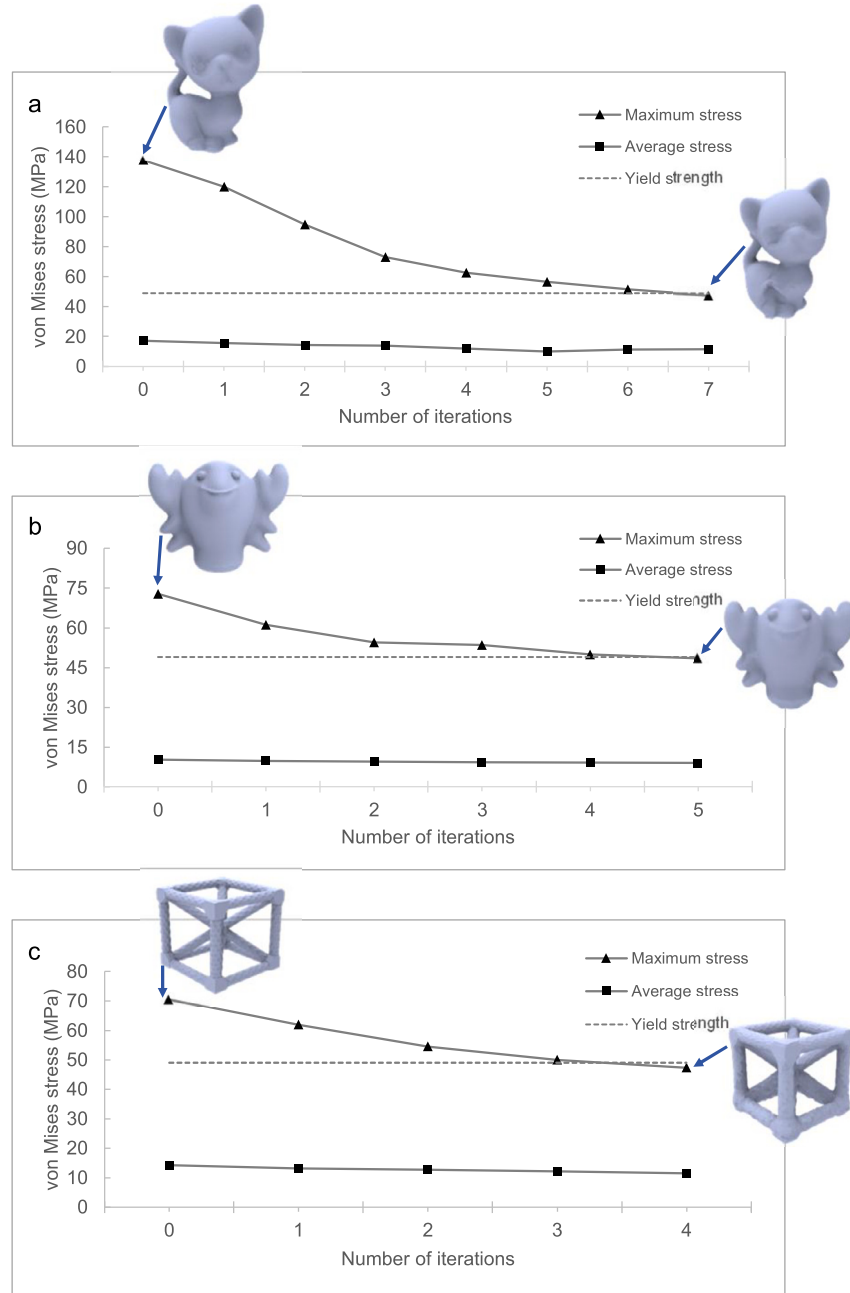


**Fig. 10. Line chart of stress variations under pressurized conditions. (a) Line chart of the Kitten model. (b) Line chart of the Wawa model. (c) Line chart of the Lattice model.** Note that the yield strength is  $S \cdot \sigma_y = 49$  MPa.

injection holes and air holes in the mould, this experiment employs the method of Jiang et al. [65]. To validate the effectiveness of the proposed design methodology, a strategy utilising 3D printing technology for the manufacturing of castings is introduced.

In this experiment, the four moulds were manufactured using the Snapmaker J1s printer with FDM technology. The process involved printing the shell model using PLA and the support using PVA (a water-soluble material), followed by dissolving the support material to produce a mould suitable for casting. LMPA was utilised as the pouring material. Liquid material was injected into the mould and allowed to solidify, after which the sacrificial shell mould was mechanically removed, resulting in the final casting. The overall manufacturing process is illustrated in Fig. 11. It is worth noting that there are various methods for removing sacrificial shell moulds. For example, dichloromethane

can be used as a solvent to dissolve the shell, making it suitable for more intricate models [65].

We fabricated moulds for the four target models under both pressurized and unpressurized conditions, as illustrated in Fig. 12. Due to equipment constraints, we printed moulds for both pressurized and unpressurized conditions, but the final casting was only performed under unpressurized conditions. The final pouring results, conducted under unpressurized conditions, are presented in the last column of Fig. 12. In addition, we also performed unpressurized casting of the Hanging Ball model, as shown in Fig. 13. The findings indicate that shell optimisation is necessary for complex geometries like the Hanging Ball model, even under static casting conditions. In its initial uniform-thickness form, the printed mould exhibited localised stress concentration in the suspension region, leading to structural instability and failure. After applying the

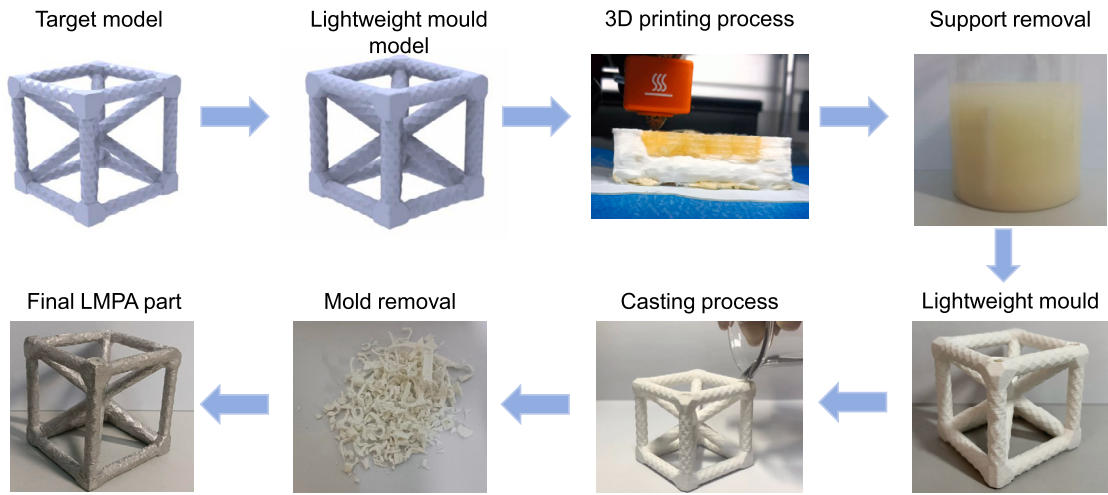


**Fig. 11.** The manufacturing process of the target casting.

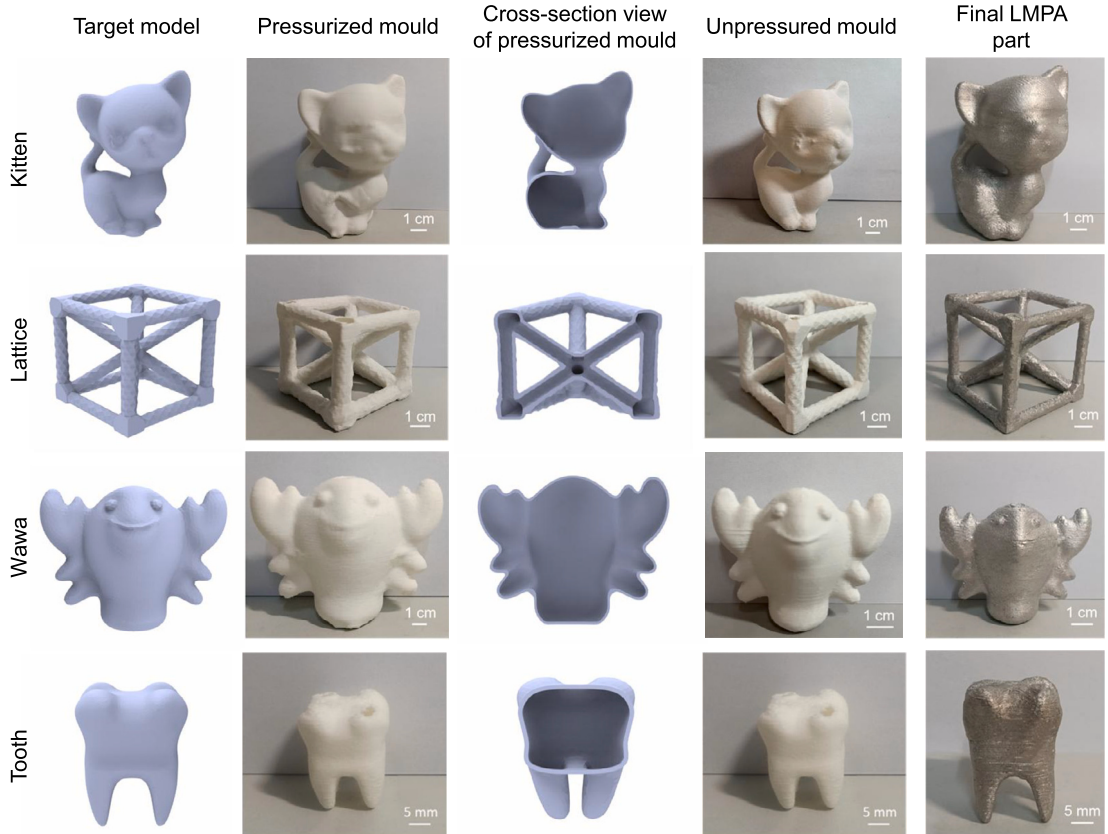


**Fig. 12. Results of model fabrication.** From left to right: Target model, pressurized mould, cross-section view of pressurized mould, unpressured mould, and final LMPA part.

proposed stress-guided optimisation, the shell was thickened in critical areas, enabling the mould to maintain integrity during unpressurized casting. These results validate that the proposed lightweight moulds are viable for practical manufacturing applications. Since the accuracy of the final products is intrinsically tied to the precision of the 3D printing process, optimising printer parameters—such as layer thickness, infill rate, and print speed—can significantly enhance the quality of the fabricated moulds. Moreover, utilising high-precision equipment or implementing post-processing techniques, such as heat treatment or surface

polishing, can further improve the surface finish and dimensional accuracy of the final manufactured parts.

### 3.3. Comparisons

To evaluate the applicability of lightweight design in 3D printed moulds, several classic models were optimised and analysed. Based on the scenarios outlined in Section 3.1, moulds were designed to suit varying manufacturing requirements and equipment types. The experimental

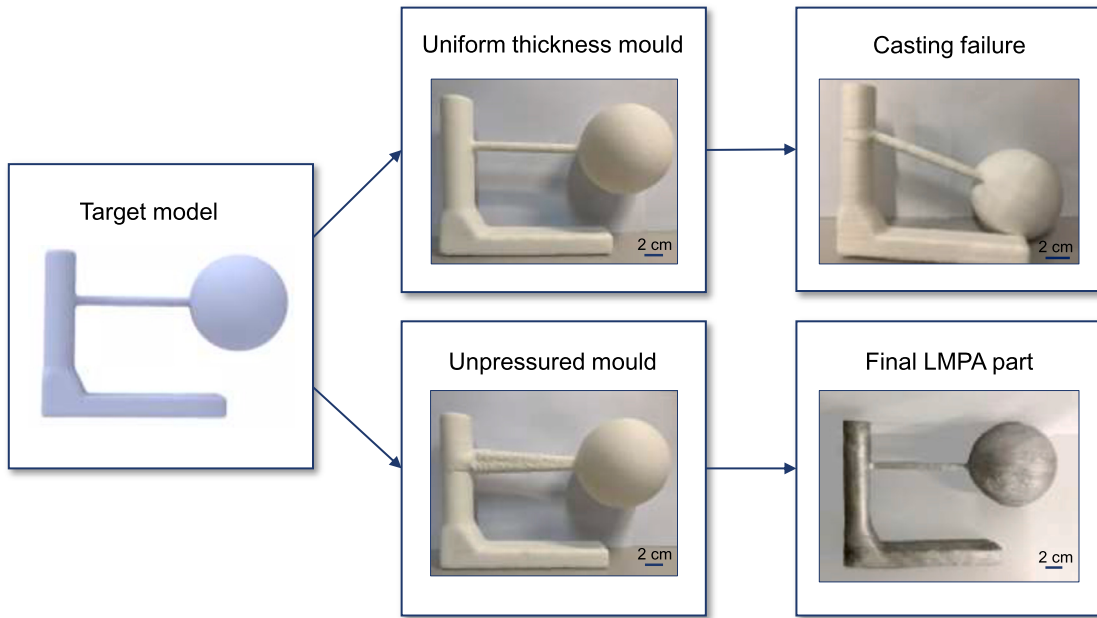


**Fig. 13.** Unpressurized casting of the Hanging Ball model.

**Table 2**

Comparison of material volume, weight, and fabrication time under unpressurized scenario.

Model	Volume [cm <sup>3</sup> ]			Weight [g]			Fabrication time [h]		
	Cube	Ours	Reduction [%]	Cube	Ours	Reduction [%]	Cube	Ours	Reduction [%]
Kitten	281.76	14.18	94.97	350.37	17.50	95.01	20.33	3.45	83.0
Lattice	116.60	12.26	89.49	143.73	13.40	90.67	9.20	3.47	62.3
Wawa	88.71	6.49	92.7	111.00	7.99	92.8	6.95	1.60	77.0
Tooth	8.90	1.92	78.4	10.70	2.26	78.9	1.12	0.72	35.7

**Table 3**

Comparison of material volume, weight, and fabrication time under pressurized scenario.

Model	Volume [cm <sup>3</sup> ]			Weight [g]			Fabrication time [h]		
	Cube	Ours	Reduction [%]	Cube	Ours	Reduction [%]	Cube	Ours	Reduction [%]
Kitten	281.76	17.79	93.69	350.37	22.01	93.72	20.33	4.05	80.1
Lattice	116.60	16.83	85.57	143.73	20.90	85.46	9.20	3.72	59.6
Wawa	88.71	6.97	92.1	111.00	8.31	92.5	6.95	1.73	75.1
Tooth	8.90	1.92	78.4	10.70	2.26	78.9	1.12	0.72	35.7

results for moulds used in manual pouring are summarised in Table 2, while Table 3 presents the results for moulds used with pressure equipment. Under these two experimental conditions, the proposed method achieves maximum reductions of 94.97%, 95.01%, and 83.0% in material consumption volume, weight, and fabrication time, respectively, when compared to a conventional cubic mould design [65].

The findings indicate that all selected models achieved substantial volume reductions compared to traditional cubic moulds. The lightweight designs demonstrated clear advantages, including significantly decreased material volume, reduced weight, and shortened fabrication time. Furthermore, the optimisation effect became increasingly pronounced with larger model sizes, highlighting the scalability and efficiency of the proposed method.

Overall, the proposed stress distribution-driven shell optimisation approach effectively accommodates diverse application scenarios. The optimised models not only reduce material consumption and fabrica-

tion time but also maintain sufficient strength and stability, even under high-pressure conditions, making them suitable for practical use.

### 3.4. Discussion

This study presents a stress-guided lightweight sacrificial mould design method that optimises shell thickness distribution to minimise material usage while maintaining structural integrity. The proposed approach is applicable to both gravity casting moulds and high-pressure casting moulds. For static injection or small-scale moulds, the design requirements can often be satisfied during the initial stage by generating a uniformly thick shell. This outcome represents a specific application of our algorithm, serving as a simplified case within its broader framework. For more complex or larger models, stress distribution requires careful consideration. For instance, the Hanging-Ball model and the Flamingo model shown in Fig. 7(a) exhibit structural characteristics that result in stress concentrations. Despite their overall dimensions being compa-

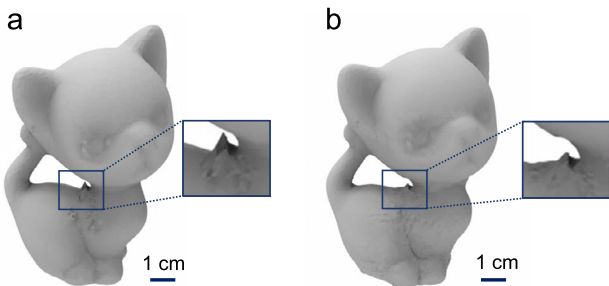


**Fig. 14. Comparison of optimisation criteria using yield stress and average stress. (a)** Optimisation using yield stress as the reference criterion. **(b)** Optimisation using average stress as the reference criterion.

able to other models, the stress at the middle connection exceeds the yield strength due to their unique geometries. Additionally, as illustrated in Fig. 7(b), the maximum stress for the same model (e.g., the Kitten model) increases progressively with size. These findings highlight the importance of stress analysis in optimising lightweight moulds for complex geometries. In high-pressure casting scenarios, lightweight mould designs can still be effectively achieved through iterative optimisation processes.

To facilitate rapid optimisation, certain simplifications were introduced. For example, this study assumed uniform material properties, a reasonable assumption for commonly used 3D printing materials such as PLA. However, in practical applications, the layered nature of the 3D printing process often results in anisotropic mechanical properties, which are not fully accounted for in the current stress analysis. Addressing this limitation will require further research to enhance the accuracy of stress modelling in the future.

The iterative optimisation method adjusts shell thickness by applying normal offsets to local nodes. To achieve an enhanced optimisation effect, the average stress is employed as a reference criterion during the optimisation process, guiding incremental adjustments to the shell thickness. This design choice is based on the observation that directly referencing the yield strength can result in an overemphasis on high-stress regions, leading to abrupt thickness variations in localised areas, as illustrated in Fig. 14(a). Such abrupt changes can adversely affect the visual appearance of the model and cause uneven stress distribution.

By contrast, utilising average stress as the guiding metric ensures balanced thickness adjustments across different nodes, resulting in smoother transitions in shell thickness, as depicted in Fig. 14(b). This approach not only produces a more uniform and optimised thickness distribution but also mitigates the risk of structural failure due to localised stress concentrations. Consequently, this method enhances the overall structural performance and reliability of the mould, making it a robust solution for lightweight sacrificial mould design under varying application conditions.

#### 4. Conclusions and future work

This paper proposes a stress-guided lightweight design method for 3D printing sacrificial moulds, addressing the challenge of material savings in sacrificial mould manufacturing. The proposed method generates a non-uniform thickness volume-level shell model based on stress distribution for mould manufacturing, while incorporating manufacturability constraints and optimising the thickness of the mould shell during the design process. Compared to traditional cube-shaped sacrificial moulds, the method achieves up to 94.7% reduction in volume, 95.01% material savings, and 83% improvement in fabrication time, all while maintaining structural stability. Additionally, a strategy for casting manufacturing using 3D printed moulds is introduced. In this strategy, PLA is employed as the primary mould material, with PVA serving as the support material. After the mould is manufactured, the water-soluble support structure is dissolved, followed by the injection of LMPA. Once

the alloy solidifies, the outer shell is removed to obtain the target model. The successful demonstration of this process validates the feasibility and effectiveness of the lightweight mould design, offering a practical and efficient technical solution for 3D printed mould users.

This method is particularly well-suited for the manufacturing of customised, small-batch, high-complexity, low-cost, and environmentally conscious components, demonstrating broad applicability across various industries. Typical application scenarios include the casting of customised automotive parts, medical devices, jewellery, artworks, and industrial components. Specifically, the proposed approach can be directly applied to eggshell casting, where stress-optimised designs enable the fabrication of ultra-thin yet structurally stable sacrificial moulds, significantly enhancing material efficiency and reducing casting defects. In the manufacturing of precision medical devices, such as joint implants and patient-specific orthotic supports, this method facilitates the production of complex-structured, mechanically robust moulds through local reinforcement and overall lightweight design, meeting the stringent requirements for accuracy and stability. Moreover, the method is also well-suited for the casting of intricate jewellery and artworks, particularly where high surface quality and detail retention are critical. Overall, the process presented in this study offers strong adaptability, allowing flexible adjustment to different material properties and specific application needs, thus exhibiting promising prospects for broader adoption. The lightweight sacrificial moulds fabricated via 3D printing provide small and medium-sized enterprises, as well as customised product manufacturers, with an economical and efficient mould-making solution to meet diverse and flexible production needs. Moreover, through significant reduction in material usage and the selection of environmentally friendly materials, the proposed method offers a sustainable alternative for resource-constrained or environmentally sensitive manufacturing environments. However, due to the limitations of the 3D printing process, the sacrificial moulds developed in this study are only suitable for casting low-melting-point materials and are not applicable to high-temperature metal casting, such as aluminium or copper, which typically exceed 600 °C. In addition, the pointwise stress-based shell thickness optimisation involves multiple rounds of FEA iterations. Although effective, this process can become computationally expensive for larger or more complex models, potentially limiting its applicability in rapid design scenarios.

Despite these contributions, several aspects need further improvement. First, although the PLA mould was successfully fabricated and the LMPA was cast into the model, the solidification process of the alloy results in volumetric shrinkage, which causes dimensional deviations in the final product geometry. To address this issue, shrinkage effects should be incorporated into the design process through compensation strategies [73]. Currently, shell thickness optimisation is primarily based on stress distribution, which has proven effective. However, real-world applications often involve more complex scenarios. To improve the precision and robustness of the design, advanced numerical and multiphysics simulation techniques could be employed. These simulations would enable more accurate predictions of the effects of solidification shrinkage and thermal stress on product geometry, allowing for proactive adjustments during the design phase to enhance the final product's accuracy. Secondly, the current mould printing process necessitates the use of internal supports, which require manual removal. Additionally, material injection for the experimental model is manually performed, resulting in inefficiencies in both manpower and time. Future work should focus on optimising the design to eliminate or minimise the need for internal supports and developing an integrated workflow that automates the processes of 3D printing and casting. By addressing these challenges, this research aims to further advance the efficiency and applicability of lightweight sacrificial mould design in industrial manufacturing contexts.

## CRediT authorship contribution statement

**Wenpeng Xu:** Writing – review & editing, Supervision, Resources, Project administration, Methodology, Funding acquisition. **Ning Zhang:** Writing – original draft, Visualization, Validation, Methodology, Investigation, Formal analysis, Data curation. **Hao Xu:** Validation, Methodology, Investigation, Formal analysis, Conceptualization. **Liuchao Jin:** Writing – review & editing, Visualization, Methodology, Investigation, Formal analysis, Conceptualization. **Jingchao Jiang:** Writing – review & editing, Supervision, Project administration, Methodology, Funding acquisition, Formal analysis, Conceptualization.

## Declaration of competing interest

The authors declare that they have no known competing financial interests or personal relationships that could have appeared to influence the work reported in this paper.

## Acknowledgements

W.X. acknowledges the support by the Natural Science Foundation of Henan (No. 242300420281 and No. 252300421511) and the Fundamental Research Funds for the Universities of Henan Province (No. NS-RRF240817). L.J. acknowledges the support by Research Grants Council (Hong Kong) under Hong Kong PhD Fellowship Scheme (No. PF21-60853).

## Data availability

The authors confirm that the data supporting the findings of this study are available within the article.

## References

- [1] S.J. Park, J.H. Lee, J. Yang, W. Heogh, D. Kang, S.M. Yeon, S.H. Kim, S. Hong, Y. Son, J. Park, Lightweight injection mold using additively manufactured Ti-6Al-4V lattice structures, *J. Manuf. Process.* 79 (2022) 759–766.
- [2] L. Jin, X. Zhai, K. Zhang, J. Jiang, W.-H. Liao, Spider Web-Inspired Additive Manufacturing: Unleashing the Potential of Lightweight Support Structures, *MATEC Web of Conferences*, vol. 401, EDP Sciences, 2024, p. 02003.
- [3] T. Alderighi, L. Malomo, T. Auzinger, B. Bickel, P. Cignoni, N. Pietroni, State of the Art in Computational Mould Design, *Computer Graphics Forum*, vol. 41, Wiley Online Library, 2022, pp. 435–452.
- [4] L.B. Hunt, The long history of lost wax casting: over five thousand years of art and craftsmanship, *Gold Bull.* 13 (2) (1980) 63–79.
- [5] F.R. Sias, Lost-Wax Casting: Old, New, and Inexpensive Methods, Woodsmere Press, 2005.
- [6] R. Sanz-Horta, S. Retegi-Carrion, R. Ruiz-Hernandez, N. Khatami, C. Elvira, E. Martinez-Campos, J. Rodriguez-Hernández, A. Abarregui, Polycaprolactone with multiscale porosity and patterned surface topography prepared using sacrificial 3D printed moulds: towards tailor-made scaffolds, *Biomater. Adv.* 151 (2023) 213465.
- [7] S. Nagarajan, H. Belaid, S. Radhakrishnan, C. Teyssier, S. Balme, P. Miele, D. Cornu, N.K. Subbaraya, V. Cavaillès, M. Bechelany, Sacrificial mold-assisted 3D printing of stable biocompatible gelatin scaffolds, *Bioprinting* 22 (2021) e00140.
- [8] P. Kumar, I.S. Ahuja, R. Singh, Experimental investigations on hardness of the biomedical implants prepared by hybrid investment casting, *J. Manuf. Process.* 21 (2016) 160–171.
- [9] G. Li, M.H.M. Marican, S.W. Gan, T. Li, L. Zhang, J. Liu, T. Li, C.C. Yen, B.W. Chua, W. Zhai, Replicating Mg scaffold via 3D printing sacrificial template, *J. Manuf. Process.* 124 (2024) 1349–1356.
- [10] S.E. Doyle, S. Duchi, C. Onofrillo, A. Quigley, C. Di Bella, E. Pirogova, C.D. O'Connell, Printing between the lines: intricate biomaterial structures fabricated via negative embodied sacrificial template 3D (NEST3D) printing, *Adv. Mater. Technol.* 6 (7) (2021) 2100189.
- [11] A. Koivikko, V. Sariola, Fabrication of soft devices with buried fluid channels by using sacrificial 3D printed molds, in: 2019 2nd IEEE International Conference on Soft Robotics (RoboSoft), IEEE, 2019, pp. 509–513.
- [12] P. Wang, J. Li, G. Wang, L. He, Y. Yu, B. Xu, Multimaterial additive manufacturing of LTCC matrix and silver conductors for 3D ceramic electronics, *Adv. Mater. Technol.* 7 (8) (2022) 2101462.
- [13] M. Goenka, C. Nihal, R. Ramanathan, P. Gupta, A. Parashar, J. Joel, Automobile parts casting-methods and materials used: a review, *Mater. Today Proc.* 22 (2020) 2525–2531.
- [14] B. Aouadi, S. Ghannem, B. Ben Fathallah, M. Yallese, Additive manufacturing and investment casting comparison of superalloys: aerospace industry, in: *Advances in Additive Manufacturing Conference*, Springer, 2023, pp. 125–131.
- [15] A. Mourya, A. Nanda, K. Parashar, R. Kumar, et al., An explanatory study on defects in plastic molding parts caused by machine parameters in injection molding process, *Mater. Today Proc.* 78 (2023) 656–661.
- [16] I. Burgués-Ceballos, P. Pinyol-Castillo, A. López-Porta, E. Pascual, T. Syrový, L. Syrova, F. Josefík, B. Dhuiège, I. Serrano, P.D. Lacharmoise, et al., Injection molding plastic solar cells, *Adv. Sci.* 10 (32) (2023) 2304720.
- [17] K. Zhang, J. Jiang, L. Jin, Q. Gao, X. Zhai, S. Zhou, Z. Li, J. Li, W.-H. Liao, Low-melting-point alloy/polyurethane auxetic composite foam for outstanding impact protection with favorable shape memory effect, *Smart Mater. Struct.* 34 (4) (2025) 045025.
- [18] D. Fan, Y. Liao, W. Wu, P. Zhang, X. Yang, R. Zhu, Y. Wang, C. Yang, H. Wang, Flow casting soft shells with geometrical complexity and multifunctionality, *Adv. Mater. Technol.* 8 (8) (2023) 2201640.
- [19] Y. Liu, Y. Pan, J. Sun, X. Wu, J. Zhang, F. Kuang, X. Lu, Metal injection molding of high-performance Ti composite using hydride-dehydride (HDH) powder, *J. Manuf. Process.* 89 (2023) 328–337.
- [20] G. Singh, J.-M. Missiaen, D. Bouvard, J.-M. Chaix, Additive manufacturing of 17–4 PH steel using metal injection molding feedstock: analysis of 3D extrusion printing, debinding and sintering, *Addit. Manuf.* 47 (2021) 102287.
- [21] H. Zhang, C. Li, Y. Li, X. Sun, Q. Li, L. Gui, Micro-casting/assembly technology based on bismuth-based liquid metal, *Adv. Mater. Technol.* (2024) 2301625.
- [22] H. Guo, X. Lv, W. Chen, Y. Zhong, W. Zou, L. Liu, H. Yu, Fabrication of a flexible strain sensor with high-aspect-ratio liquid-metal Galinstan, *Adv. Mater. Technol.* 8 (1) (2023) 2200749.
- [23] A.A. Luo, A.K. Sachdev, D. Apelian, Alloy development and process innovations for light metals casting, *J. Mater. Process. Technol.* 306 (2022) 117606.
- [24] B. Zhao, S. Xing, W. Gao, G. Yan, Effect of pressure on the microstructure refinement, solidification mechanism and fracture behavior of wrought Al-Zn-Mg-Cu alloys prepared by squeeze casting, *J. Mater. Process. Technol.* 324 (2024) 118239.
- [25] H. Xie, J. Wang, Y. Li, J. Song, H. Hu, L. Qin, H. Zhao, C. Li, Y. Cui, Z. Tan, et al., Fast shot spot induced microstructure and mechanical property evolution of high pressure die casting Mg-Al-Zn-RE alloys, *J. Mater. Process. Technol.* 331 (2024) 118523.
- [26] G.-C. Chen, X. Li, Effect of tic nano-treating on the fluidity and solidification behavior of aluminum alloy 6063, *J. Mater. Process. Technol.* 324 (2024) 118241.
- [27] Q. Li, G. You, X. Ling, P. Zhou, L. Wang, J. Feng, S. Zeng, X. Tong, B. Jiang, Enhancing fusion welding in die-cast mg alloys: a combined ultrasonic vibration and hot rolling approach for porosity reduction, microstructure refinement, and mechanical property improvement, *J. Mater. Process. Technol.* 331 (2024) 118513.
- [28] A.A. Hassen, M. Noakes, P. Nandwana, S. Kim, V. Kunc, U. Vaidya, L. Love, A. Nyct, Scaling up metal additive manufacturing process to fabricate molds for composite manufacturing, *Addit. Manuf.* 32 (2020) 101093.
- [29] Y.-P. Zhang, C.-G. Zhou, W.-J. Sun, T. Wang, L.-C. Jia, D.-X. Yan, Z.-M. Li, Injection molding of segregated carbon nanotube/polypropylene composite with enhanced electromagnetic interference shielding and mechanical performance, *Compos. Sci. Technol.* 197 (2020) 108253.
- [30] J. Zhao, Y. Qiao, G. Wang, C. Wang, C.B. Park, Lightweight and tough PP/talc composite foam with bimodal nanoporous structure achieved by microcellular injection molding, *Mater. Des.* 195 (2020) 109051.
- [31] Z. Mirzazadeh, Z. Sherafat, E. Bagherzadeh, Physical and mechanical properties of pdvf/knn composite produced via hot compression molding, *Ceram. Int.* 47 (5) (2021) 6211–6219.
- [32] M.Y. Khalid, Z.U. Arif, M.F. Sheikh, M.A. Nasir, Mechanical characterization of glass and jute fiber-based hybrid composites fabricated through compression molding technique, *Int. J. Mater. Form.* 14 (5) (2021) 1085–1095.
- [33] D. Tachibana, K. Matsubara, R. Matsuda, T. Furukawa, S. Maruo, Y. Tanaka, O. Fuchiwaki, H. Ota, 3D helical micromixer fabricated by micro lost-wax casting, *Adv. Mater. Technol.* 5 (1) (2020) 1900794.
- [34] L. Xu, Z. Li, H. Lu, X. Qi, Y. Dong, H. Dai, Z. Islam Md, Y. Fu, Q. Ni, Electrothermally-driven elongating-contracting film actuators based on two-way shape memory carbon nanotube/ethylene-vinyl acetate composites, *Adv. Mater. Technol.* 7 (7) (2022) 2101229.
- [35] J.-T. Miao, M. Ge, Y. Wu, S. Peng, L. Zheng, T.Y. Chou, L. Wu, 3D printing of sacrificial thermosetting mold for building near-infrared irradiation induced self-healable 3D smart structures, *Chem. Eng. J.* 427 (2022) 131580.
- [36] E. Cisneros-López, A. Pal, A. Rodriguez, F. Wu, M. Misra, D. Mielewski, A. Kiziltas, A. Mohanty, Recycled poly (lactic acid)-based 3D printed sustainable biocomposites: a comparative study with injection molding, *Mater. Today Sustain.* 7 (2020) 100027.
- [37] W. Xu, H. Xu, X. Zhai, J. Jiang, Nature-inspired interlaced printing strategies for additive manufacturing highly improved mechanical properties, *Addit. Manuf.* 89 (2024) 104276.
- [38] J. Ye, A. El Desouky, A. Elwany, On the applications of additive manufacturing in semiconductor manufacturing equipment, *J. Manuf. Process.* 124 (2024) 1065–1079.
- [39] J. Zhao, Y. Yang, M.H. Kobir, J. Faludi, F. Zhao, Driving additive manufacturing towards circular economy: state-of-the-art and future research directions, *J. Manuf. Process.* 124 (2024) 621–637.

- [40] W. Xue, L. Jin, B. Jian, Q. Ge, Origami-based flexible robotic grippers via hard-soft coupled multimaterial 3D printing, *Soft Robot.* (2025).
- [41] N. Karimi, H. Fayazfar, Development of highly filled nickel-polymer feedstock from recycled and biodegradable resources for low-cost material extrusion additive manufacturing of metals, *J. Manuf. Process.* 107 (2023) 506–514.
- [42] H. Xu, C. Liu, H. Mao, F. Bai, T. Xu, Strengthening nodes to obtain high-strength pyramid lattice structure by using wire arc additive manufacturing method, *J. Manuf. Process.* 117 (2024) 125–133.
- [43] L. Jin, X. Zhai, K. Zhang, J. Jiang, W.-H. Liao, 3D printing soft robots integrated with low-melting-point alloys, *Mater. Sci. Addit. Manuf.* 3 (3) (2024) 4144.
- [44] J.D. Berrio Bernal, E.C. Silva, W. Montealegre Rubio, Characterization of effective Young's modulus for fused deposition modeling manufactured topology optimisation designs, *Int. J. Adv. Manuf. Technol.* 103 (2019) 2879–2892.
- [45] D.C. Ackland, D. Robinson, M. Redhead, P.V.S. Lee, A. Moskaljuk, G. Dimitroulis, A personalized 3D-printed prosthetic joint replacement for the human temporomandibular joint: from implant design to implantation, *J. Mech. Behav. Biomed. Mater.* 69 (2017) 404–411.
- [46] T. Sathish, M. Vijayakumar, A.K. Ayyangar, Design and fabrication of industrial components using 3D printing, *Mater. Today Proc.* 5 (6) (2018) 14489–14498.
- [47] L. Jin, S. Yu, J. Cheng, Z. Liu, K. Zhang, S. Zhou, X. He, G. Xie, M. Bodaghi, Q. Ge, W.-H. Liao, Machine learning powered inverse design for strain fields of hierarchical architectures, *Composites Part B, Engineering* 299 (2025) 112372.
- [48] L. Jin, S. Yu, J. Cheng, H. Ye, X. Zhai, J. Jiang, K. Zhang, B. Jian, M. Bodaghi, Q. Ge, W.-H. Liao, Machine learning driven forward prediction and inverse design for 4D printed hierarchical architecture with arbitrary shapes, *Appl. Mater. Today* 40 (2024) 102373.
- [49] B. Sheng, F. Zhao, X. Yin, C. Zhang, H. Wang, P. Huang, A lightweight surface reconstruction method for online 3D scanning point cloud data oriented toward 3D printing, *Math. Probl. Eng.* 2018 (1) (2018) 4673849.
- [50] J.-W. Kang, Q.-X. Ma, The role and impact of 3D printing technologies in casting, *China Foundry* 14 (2017) 157–168.
- [51] C. Deng, J. Kang, H. Shangguan, Y. Hu, T. Huang, Z. Liu, Effects of hollow structures in sand mold manufactured using 3D printing technology, *J. Mater. Process. Technol.* 255 (2018) 516–523.
- [52] M. Gao, L. Li, Q. Wang, Z. Ma, X. Li, Z. Liu, Integration of additive manufacturing in casting: advances, challenges, and prospects, *Int. J. Precis. Eng. Manuf. Green Technol.* (2022) 1–18.
- [53] L. Jin, X. Zhai, K. Zhang, J. Jiang, Unlocking the potential of low-melting-point alloys integrated extrusion additive manufacturing: insights into mechanical behavior, energy absorption, and electrical conductivity, *Prog. Addit. Manuf.* (2024) 1–13.
- [54] Z. Liu, W. Zhang, X. Gan, F. Yan, J. Wang, C. Wang, Mechanism of regulating surface morphology and microstructure in laser polishing of mold steel through pulse spatiotemporal distribution, *J. Manuf. Process.* 126 (2024) 252–266.
- [55] X. Zhou, T. Yuan, Y. Xu, Complex-shaped titanium components fabricated via metal injection molding using hydride-dehydride titanium powder, *J. Manuf. Process.* 126 (2024) 220–229.
- [56] C.-C. Kuo, P.-H. Lin, J.-Y. Xu, Z.-X. Lin, Z.-H. Wang, S.-H. Huang, Polymeric advancements in innovating wax injection molds using aluminum-filled epoxy resin with face-cooled waterfall cooling channels, *J. Manuf. Process.* 124 (2024) 954–965.
- [57] J. Gim, H. Yang, L.-S. Turng, Transfer learning of machine learning models for multi-objective process optimisation of a transferred mold to ensure efficient and robust injection molding of high surface quality parts, *J. Manuf. Process.* 87 (2023) 11–24.
- [58] C.-C. Kuo, Q.-Z. Tasi, B.-X. Xie, J.-M. Huang, S.-X. Qiu, Improving the quality of a circular cooling channel fabrication by fused filament fabrication using Taguchi methods, *Int. J. Adv. Manuf. Technol.* 120 (5) (2022) 3353–3364.
- [59] C.-C. Kuo, J.-Y. Chen, Y.-H. Chang, Optimisation of process parameters for fabricating polylactic acid filaments using design of experiments approach, *Polymers* 13 (8) (2021) 1222.
- [60] M. Harris, H. Mohsin, J. Potgieter, K. Ishfaq, R. Archer, Q. Chen, K. De Silva, M.-J.L. Guen, R. Wilson, K.M. Arif, Partial biodegradable blend with high stability against biodegradation for fused deposition modeling, *Polymers* 14 (8) (2022) 1541.
- [61] J. Andrzejewski, M. Gronkowski, J. Anisko, A novel manufacturing concept of LCP fiber-reinforced GPET-based sandwich structures with an FDM 3D-printed core, *Materials* 15 (15) (2022) 5405.
- [62] R. Vahed, H.R. Zareie Rajani, A.S. Milani, Can a black-box AI replace costly DMA testing?—a case study on prediction and optimisation of dynamic mechanical properties of 3D printed acrylonitrile butadiene styrene, *Materials* 15 (8) (2022) 2855.
- [63] J. Montero, P. Vitale, S. Weber, M. Bleckmann, K. Paetzold, Indirect additive manufacturing of resin components using polyvinyl alcohol sacrificial moulds, *Proc. CIRP* 91 (2020) 388–395.
- [64] R. Wick-Joliat, M. Tschauder, R. Kontic, D. Penner, Water-soluble sacrificial 3D printed molds for fast prototyping in ceramic injection molding, *Addit. Manuf.* 48 (2021) 102408.
- [65] J. Jiang, X. Zhai, K. Zhang, L. Jin, Q. Lu, Z. Shen, W.-H. Liao, Low-melting-point alloys integrated extrusion additive manufacturing, *Addit. Manuf.* 72 (2023) 103633.
- [66] S. Liu, C.C. Wang, Fast intersection-free offset surface generation from freeform models with triangular meshes, *IEEE Trans. Autom. Sci. Eng.* 8 (2) (2010) 347–360.
- [67] W. Jung, H. Shin, B.K. Choi, Self-intersection removal in triangular mesh offsetting, *Comput.-Aided Des. Appl.* 1 (1–4) (2004) 477–484.
- [68] J. Etienne, N. Ray, D. Panizzo, S. Hornus, C.C. Wang, J. Martínez, S. McMains, M. Alexa, B. Wyvill, S. Lefebvre, Curvislicer: slightly curved slicing for 3-axis printers, *ACM Trans. Graph.* 38 (4) (2019) 1–11.
- [69] X. Guidetti, E.C. Balta, Y. Nagel, H. Yin, A. Rupenyan, J. Lygeros, Stress flow guided non-planar print trajectory optimisation for additive manufacturing of anisotropic polymers, *Addit. Manuf.* 72 (2023) 103628.
- [70] L. Robles-Lorite, R. Dorado-Vicente, A. García-Collado, E. Torres-Jiménez, Procedure to improve the surface fidelity of additive manufactured parts via direct slicing tessellation, *Expert Syst. Appl.* 242 (2024) 122822.
- [71] W. Xu, H. Xu, Q. Li, P. Zhang, L. Yang, W. Wang, Stress-based continuous planar path planning for additive manufacturing, *Adv. Eng. Softw.* 188 (2024) 103544.
- [72] H. Nunes, O. Emadinia, M.F. Vieira, A. Reis, Low- and high-pressure casting aluminum alloys: a review, in: S. Rajendrachari (Ed.), *Recent Advancements in Aluminum Alloys*, IntechOpen, Rijeka, 2023, Ch. 4.
- [73] J. Jiang, X. Zhai, L. Jin, K. Zhang, J. Chen, Q. Lu, W.-H. Liao, Design for reversed additive manufacturing low-melting-point alloys, *J. Eng. Des.* (2023) 1–14.